

# We are IntechOpen, the world's leading publisher of Open Access books Built by scientists, for scientists

4,800

Open access books available

122,000

International authors and editors

135M

Downloads

Our authors are among the

154

Countries delivered to

TOP 1%

most cited scientists

12.2%

Contributors from top 500 universities



WEB OF SCIENCE™

Selection of our books indexed in the Book Citation Index  
in Web of Science™ Core Collection (BKCI)

Interested in publishing with us?  
Contact [book.department@intechopen.com](mailto:book.department@intechopen.com)

Numbers displayed above are based on latest data collected.  
For more information visit [www.intechopen.com](http://www.intechopen.com)



# Nanoplasmonic for Solar Energy Conversion Devices

*Samy K.K. Shaat, Hussam Musleh, Jihad Asad,  
Nabil Shurrab, Ahmed Issa, Amal AlKahlout and  
Naji Al Dahoudi*

## Abstract

The effect of nanoplasmonic (Ag) on the performance of DSSCs has been studied in doped and undoped ZnO (DZ and UZ) NPs, which were prepared by the urea-assisted combustion route. Different techniques were conducted to characterize DZ and UZ NPs. XRD patterns were indexed to the hexagonal wurtzite structure of ZnO NPs (ICSD-52362). The values of average crystalline size of UZ and DZ (1.0 mol% Ag) NPs were 20.45 and 22.30 nm, respectively. HR-TEM micrograph revealed good crystallization with an intermediate or poor agglomeration with distribution of semispherical morphologies of ZnO NPs. The energy bandgap of UZ and DZ NPs was changed from 3.21 to 3.31 eV. The deconvolution of the PL spectra recognized eight peaks into near ultraviolet (NUV) and visible regions. The PL emission of visible region overshadowed NUV transition. The photovoltaic cell with the doped photoanode DZ:1.0 mol% Ag exhibited the best performance parameters:  $V_{oc} = 0.46$  V,  $J_{sc} = 7.81$  mA.cm<sup>-2</sup>,  $P_m = 1.91$ , FF = 51%, and  $\eta = 1.91\%$ . A double exponential function was used as a powerful fitting function for the TOCVD data. The results revealed that  $\tau_n$  in the UZ NPs photoanode was longer than that in the DZ:1.0 mol% Ag NPs photoanode.

**Keywords:** combustion synthesis, eosin Y, nanoplasmonic, solar energy conversion device, renewable energy, defects, lifetime, electron recombination

## 1. Introduction

The exacerbation of energy worldwide crisis in addition to two bottlenecks: (i) the inevitable exhaustion of fossil fuel in the coming fifty years and (ii) the global environmental damage caused by the combustion of large amounts of fossil fuels [1], spurs us to find a new pollution-free, eco-friendly, renewable, clean and sustainable energy source [2]. There are many types of renewable energy resources—such as wind, biomass, and tidal, geothermal, and solar energy [3]. Accordingly, solar energy has been increasingly exploited, which is the most promising one to meet the future demands as it is in limitless supply [2]. Consequently, it is imperative to develop solutions to broaden light absorption and suppress charge recombination toward efficient solar energy conversion (SEC) [2]. Hence, SEC into a most usable form, i.e., electrical energy, is highly important to fulfill the ever-increasing demand for energy [1]. Photoelectrical conversion (PEC) is a promising

and environmentally friendly technology to solve the energy crisis faced because sunlight gives a power of 106 TW/year continuously [4]. Photovoltaic cells (PVs) are an essential component in smart grids and mobile commerce or in the development of integrated photovoltaics (BIPVs) and vehicles [5]. Dye-sensitized solar cells (DSSCs) are a class of mesoporous solar device which have evolved as credible alternative to conventional solid-state p-n junction photovoltaics [6, 7]. The DSSCs have several advantages, showing higher performance with relatively lower cost, lower handling expenses, lower strength of optical and incidence angles, higher mechanical durability, lighter weight, and more aesthetically pleasing and transparent design [1, 5]. With the advantages of being easily manufactured, colored, and flexible, this type of solar cells has become available and considerable for reducing the cost of electricity generation [8]. Nevertheless, their low efficiencies remain a major roadblock to commercialization in DSSCs [5]. In addition, light absorption, charge recombination, and dye pickup are still a challenge in the field of DSSC technology [9]. Numerous strategies have been investigated to enhance PCE of DSSC by improvement of light harvesting, carrier collection and noble metal NPs, using semiconductor quantum dots, developing new dyes and designing new morphology [10]. Moreover, different approaches were designed such as large surface area mesoporous photoanode; hierarchically Nano-structured and scattering top-layer photoanode; new panchromatic absorbing dyes; photonic crystal photoanode and plasmonic photoanode [5, 6]. In PEC, semiconductors play an important role in capturing light to generate electron-hole pairs for subsequent electricity and chemical fuel production. Also, they generate photocurrent and produce  $H_2$  under visible light illumination [4]. Recent researches on pure and alloyed metal NPs demonstrated high potential in this field to improve light absorption/scattering properties of semiconductor network. This is due to their unique response under particular wavelengths known as plasmonic effect [9]. Newly, ZnO has been used as an alternative n-type semiconducting photoanode material for DSSCs. This is because ZnO has high electron dynamics, and a versatile nanostructure morphology relative to others [11]. ZnO plays an important role in the optoelectronic devices. This is because of its excellent properties of piezoelectric, electron conductivity, and a large exciton binding energy of 60 meV [12]. One general advantage of incorporating NPs into DSSCs is that they provide far-field scattering and concomitant enhancement. This is due to longer effective optical path lengths [13]. Their outstanding light trapping and electromagnetic field concentrating properties proved very effective [9]. Further modifications have been performed by mixing with other nanostructured metal oxides or with metallic NPs. These metallic NPs include noble metals (NMs) Au, Ag, and Cu, i.e., nanoplasmonic (NPL) metals), for improving their charge carrier and absorption properties [11]. NMs in nanoscale have widely been applied in various research fields, including optical sensors, catalysts, and surface-enhanced Raman scattering. This is due to their characteristic optical and electrical properties, which are not available with bulk analogues [14]. NPL has unique optical characteristics that can be harnessed for several technological applications from spectroscopy to nanomedicine to photovoltaics [7]. NPL is a rapidly growing research field that exploits enhancement of concentrated optical energy on the nanoscale in nanostructured metal [11]. Also, NPL enhanced photocatalytic including water splitting, artificial photosynthesis, and photodegradation of organic pollutant and photovoltaic systems [2, 4, 13]. On the other hand, NPL introduction in photoactive layers of DSSC, to trap or confine light inside the active layer and enhance the absorption in the semiconductor film could provide superior performances presumably due to their unique electronic, optical and magnetic properties [15]. Moreover, NPL enhancement in solar cells is achieved by four possible mechanisms. They are far-field coupling of scattered

light, which can be trapped in the mesoporous semiconductor, near-field coupling of electromagnetic fields, plasmon resonance energy transfer from nanostructures to semiconductor, and hot-electron transfer [4, 7, 14]. As sun light possesses less energetic photons, the hot electrons cannot be produced just by the solar spectrum. In DSSC technology, this problem can be solved by the use of exothermic chemical processes [9]. In another study, quantum capacitance-like effect has been observed in the device, which accelerates the carrier transport via additional electric field [9]. The enhanced electromagnetic field is highly dependent upon the wavelength of incident light, also, the shape, size, and aggregation state of the NPs [10]. The increasing of the light-harvesting efficiency was done by introducing NPL structures into various types of PVs such as silicon, thin-film, organic solar, and polymer solar cell [10, 11, 13, 14]. Among the NMs silver, which have the critical advantages and is considered as one of the most suitable candidates for practical applications due to its facile easy preparation and lower cost than others [10]. As to the electrical aspect, Ag NPs could play a role as the electron transport separation center, which accelerated the electron to move through the photoanode network and reduced the charge recombination [8]. However, the exact mechanism for the plasmon-induced charge separation process in plasmonic photovoltaic devices is not clarified yet [14]. In conclusion, the possibility of photosensitization of MOs using plasmonic metal NPs is tantalizing [7]. While there is increasing evidence for hot-electron injection, there is no consensus to date. Further research is necessary to establish more firmly the possibility [4]. More work is also needed to better understand what factors determine the mechanism of operation. The strength of interaction between the metal NP and MOs is likely a critical factor, which may in turn depends on the detailed structures of both constituents down to the molecular or atomic level [4]. The merits designate the implementation of plasmonic nanostructures into photocatalysis and photovoltaics as a promising strategy for solar energy conversion [2]. Several methods have been reported to deposit Ag NPs onto DSSC photoanode. However, none is able to prevent the aggregation of Ag NPs and keep structures uniform during the deposition process [10]. Until now, there has been strong controversy regarding the role of plasmonic NPs in DSSCs. In addition, more in-depth investigation for the enhancement mechanism is still required [14]. Guided by this principle, in this study, we designed a kind of unique Ag-doped ZnO NPs as a photoanode in DSSCs, to investigate the plasmonic effects and elucidate the working principle more systematically. Nevertheless, this method has never been used for doping metallic particles for plasmon effect in DSSCs. The present work is the first effort to employ solution combustion method for enhancing plasmon effect in DSSCs. The plasmonic effect of Ag on the performance of DSSCs has been studied. A dramatic increase in efficiency is achieved in the device of Ag NPs/ZnO NPs compared with that of ZnO NPs.

## **2. Practical and experimental techniques**

### **2.1 Synthesis of ZnO nanoparticles**

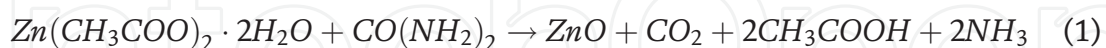
Doped and undoped (i.e., pristine sample which was used as a control specimen) ZnO (DZ and UZ) NPs were prepared by the urea-assisted combustion route. The detailed synthesis of DZ and UZ NPs has been reported elsewhere [16]. Zinc acetate (ZA) dihydrate, ( $\text{Zn}(\text{CH}_3\text{COO})_2 \cdot 2(\text{H}_2\text{O})$ ) assay  $\geq 98.9\%$ , Merck Co.), urea (U), ( $\text{CO}(\text{NH}_2)_2$ , assay  $\geq 99.9\%$ , Merck Co.), and silver nitrate  $\text{AgNO}_3$  (SN) were used as starting materials (precursors). They were utilized as purchased without further purification. The distilled water (DW) was employed to dissolve





**Figure 1.**  
A schematic illustration of the synthesis procedure of UZ and DZ NPs.

stoichiometric amounts of ZA (solutions A) and U (solutions B). Solutions A and B were stirred vigorously for 15 min at room temperature. After that, the two solutions A and B were mixed to produce solution C. A transparent homogeneous solution C was stirred vigorously for 15 min at 60°C in a beaker and was sonicated for 30 min. Solution C was transferred to a muffle furnace maintained at a temperature of  $500 \pm 10^\circ\text{C}$ . Solution C started to boil and undergo dehydration. Due to the exothermic nature of this process, a large amount of heat escaped with a huge flame. In meantime, further decomposition of the reagents and liberating more gases during the evaporation of liquid were happened. After 1 min, the flame damped, and the combustion reaction was accomplished within 5 min. White foamy and voluminous ash was achieved after spontaneous ignition occurred and underwent smoldering combustion with enormous swelling. The product ash was left to cool down to room temperature. Then, white ash was grounded gently into fine powders using a pestle and mortar:



The same producers were repeated to prepare the UZ and DZ NPs with different molar concentration of Ag (0.5, 1.0, 1.5, and 5.0%). The obtained powders were characterized without any further post-preparation treatment. The scheme for the synthesis techniques of the DZ and UZ NPs is illustrated schematically in **Figure 1**. The chemical reaction to derive ZnO NPs from solution combustion-assisted urea is written in Eq. (1).

## 2.2 Fabrication and assembly of the DSSCs devices

The as-synthesized DZ and UZ NPs (which was designed as a reference photoanode) were consumed to fabricate the working electrode (WE) for DSSCs. Two slurry pastes were prepared by mixing a small quantity of the as-synthesized DZ and UZ NPs with polyethylene glycol 400 (PEG 400) and absolute ethanol using a mortar and pestle for 12 min. The obtained homogenous pastes were layered on fluorine-doped tin oxide (FTO) substrates (Sigma-Aldrich, sheet resistance

$7 \Omega/\text{cm}^2$ ) by doctor blade technique. FTO substrates were washed using ethanol and DW several times followed by ultra-sonication using acetone for 15 min. The coated FTO substrates were heated at  $450^\circ\text{C}$  for 45 min. The estimation thickness of the heated layers was  $1215 \mu\text{m}$  with an active covered area  $0.25 \text{ cm}^2$ . In this stage, the derived photoanodes from DZ and UZ NPs were fabricated. The fabricated photoanodes were, separately, immersed in eosin Y (EY) dyes. After 24 h, the dyed photoanodes were rinsed in absolute ethanol and were dried in air at room temperature. Finally, the different DSSC devices were assembled by fixing the WE (A Pt-coated FTO substrate) and the counter electrode by paper clips with a spacer between the two electrodes. After that, the redox electrolyte solution was injected between the two electrodes to filling the space. The filling redox electrolyte solution (I-/I-3) was composed of 32 mL p-carbonate, 8 mL acetonitrile, 0.253 g iodine ( $\text{I}_2$ ), and 2.672 g lithium iodide. At last, the fabricated DSSC devices were used to measurements.

### 2.3 Characterization technique

Different techniques were conducted to characterize the as-synthesized DZ and UZ NPs. Crystal identification and crystal size analysis were tested by X-ray diffractometer (XRD), Philips Expert, where Cu-K $\alpha$  radiation ( $\lambda = 1.5418 \text{ \AA}$ ) monochromatic by a nickel filter. The values of diffraction angle ( $2\theta$ ) range from  $15^\circ$  to  $80^\circ$  and scan rate about  $0.02 \text{ s}^{-1}$ . The nanostructures and their lattice images were possessed with a 200 kV high-resolution transmission electron microscopy (HR-TEM) (JEM-2100), 200 kV. Samples for HR-TEM studies were prepared by placing a drop of nanosuspension on a carbon-coated Cu grid, and the solvent was evaporated at room temperature. Double-beam UV-Vis spectrophotometer (Shimadzu UV-1601 PC) was used to carry out the absorption spectra of synthesized UZ and DZ NPs and the absorption of sensitizing dye in the range from 300 to 800 nm in ethanolic solution. Photoluminescence (PL) emission measurements were performed at room temperature in absolute ethanol over the range from 300 to 800 nm with excitation wavelength 320 nm using (SPF-200, Biotech Engineering Management Co., UK) spectrofluorometer with 150 W xenon lamp with a high-sensitivity photomultiplier tube.

### 2.4 Measurement techniques

The photovoltaic characteristics of the fabricated DSSCs were executed under focusing irradiation using white light (40 W Xenon arc lamp) in ambient atmosphere. In addition, they were simulated with AM 1.5 sunlight illumination with an output power of  $100 \text{ mWcm}^{-2}$ . The characteristic curves of the current and the voltage (I-V) of the fabricated cells were carried out by applying an external reverse bias voltage in the range of  $-1$  to  $1 \text{ V}$  of the solar cell. A personal computer (PC) was connected to Elvis National Instruments (ENI) in combination with a LabVIEW program to collect the data of I-V characteristic curves. The transient open-circuit photovoltage (TOCPV) decay experiment was conducted by monitoring the subsequent decay. This was due to the light source being turned off after illuminating the DSSC devices based on the of  $0.32 \text{ mM}$  EY dye for 5 min. UV-Vis spectrophotometer double-beam Shimadzu UV-1601 PC with a diffraction grating with a self-aligning was equipped to measure the dye concentration of the desorbed-dye solution as described in the previous work [2]. A deuterium lamp covered the UV where a halogen lamp was the source of the visible region. The colored photoanode was immersed in a  $0.1 \text{ M}$  NaOH solution of water and ethanol (1:1, v/v).

### 3. Analysis and result discussion

#### 3.1 X-ray diffraction pattern study

XRD technique was used to investigate the crystallography structure phase and lattice parameters of the as-synthesized samples UZ and DZ (1.0 mol % Ag) NPs. **Figure 2** depicts the intense and crystalline XRD patterns of the as-synthesized samples UZ and DZ (1.0 mol% Ag) NPs, which were registered at room temperature. All the diffraction peaks are indexed to the standard hexagonal wurtzite structure of ZnO NPs (inorganic crystal structure database number ICSD-52362). The sharpness of the broadened XRD diffraction peaks is an indication of the small size and the good crystallinity of the NPs, whereas the crystallinity of DZ (1.0 mol % Ag) NPs is better than UZ NPs. In addition, no peak corresponding to any impurity could be seen, and this confirms the formation of single phase of ZnO NPs. Moreover, no peak indicates the existence of other phase of Ag NPs. It was reported that no Ag peaks could be observed for 1% and 3% Ag concentrations; however, Ag peaks can still be detected in the XRD pattern of ZnO:5% Ag NPs [17]. Furthermore, XRD peaks related to Ag were presented in the samples calcined at 500, 700, and 900°C but disappear at 1100°C calcination temperature. This reveals that Ag atoms may have diffused in ZnO matrix. It can be noted that the preferred orientation corresponding to the plane (101), which overwhelms the other peaks, is the most prominent peak, which agrees with the results of Kumar et al. [18]. The XRD diffraction peaks are significantly broadened due to the small size of the NPs [19]. The calculated lattice parameters ( $a$ ,  $c$ , and  $c/a$ ) of samples UZ and DZ (1.0 mol% Ag) NPs are listed in **Table 1**. The calculated parameters match with the results of Xiaofeng Zhou et al. [20] and H. Zayed et al. [21]. Based on the Scherrer equation, the estimated average crystallite size ( $D$ ) of the samples DZ and UZ NPs has been calculated from the highest diffraction peak along the (101) plane [22]:

$$D = \frac{k \lambda}{\beta \cos(\theta)} \quad (2)$$

where  $k$  is the particle shape factor ( $k = 0.9$  for spherical particle),  $\lambda$  is the Cu-K $\alpha$  X-ray wavelength (0.15418 nm),  $\beta$  is the full width at half maximum (FWHM) of XRD peaks, and  $\theta$  is the Bragg angle corresponding to the same plane which obtained from the diffraction angle ( $2\theta$ ). The calculated values of  $D$  of the

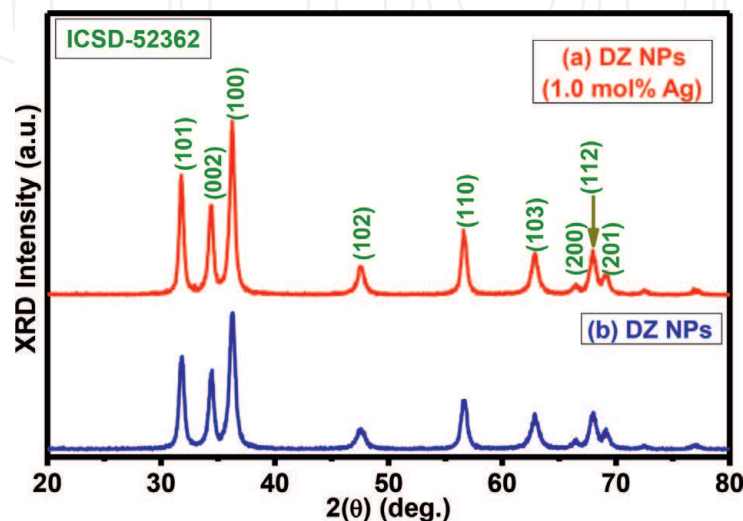


**Figure 2.**  
X-ray diffraction patterns the samples UZ and DZ (1.0 Mol% Ag) NPs.

| Sample         | (hkl) | (2 $\theta$ ) | FWHM  | c (nm) | a (nm) | c/a   | d <sub>hkl</sub> (nm) | D (nm) |        |
|----------------|-------|---------------|-------|--------|--------|-------|-----------------------|--------|--------|
|                |       |               |       |        |        |       |                       | XRD    | HR-TEM |
| UZ             | 100   | 31.804        | 0.592 | 0.325  | 0.562  | 1.731 | 0.126                 | 20.55  | 22     |
|                | 002   | 34.419        | 0.667 |        |        |       | 0.147                 |        |        |
|                | 101   | 36.261        | 0.707 |        |        |       | 0.203                 |        |        |
| DZ 1.0 mol% Ag | 100   | 31.804        | 0.523 | 0.325  | 0.563  | 1.731 | 0.281                 | 23.02  | 24     |
|                | 002   | 34.419        | 0.614 |        |        |       | 0.260                 |        |        |
|                | 101   | 36.261        | 0.621 |        |        |       | 0.247                 |        |        |

**Table 1.**  
 Geometric parameters of the samples UZ and DZ (1.0 mol% Ag) NPs.

samples UZ and DZ (1.0 mol% Ag) NPs are given in **Table 1**, which are 20.45 and 22.30 nm, respectively.

### 3.2 HR-TEM analysis

HR-TEM bright-field photomicrographs were used to determine the actual shape and size distribution of the as-synthesized samples UZ and DZ (1.0 mol% Ag) NPs. Therefore, it is important to know that the differences in the NP size and the dense distribution were used to explain these phenomena. Indeed, the larger size and highly dense distribution of Ag NPs mean that they could not preferentially attach to specific sites on the photoanode surface, resulting in a decrease of the catalytic activity [23]. **Figures 3** and **4** depict the HR-TEM micrograph of the samples UZ and DZ (1.0 mol% Ag) NPs, respectively. As revealed in **Figure 3A** and **4A**, the HR-TEM micrograph suggests that ZnO NPs are, well, crystallized with an intermediate or poor agglomeration. Moreover, as presented in **Figure 3A** and **4A**, the HR-TEM images show the distribution of semispherical morphologies of ZnO NPs. The selected area electron diffraction (SAED) patterns of samples UZ and DZ (1.0 mol% Ag) NPs are illustrated in **Figure 3B** and **4B**. This confirms the crystalline nature of the ZnO NPs. Five bright concentric diffraction rings in the SAED can be indexed as the (100), (002), (101), (102), and (110) planes of the wurtzite ZnO. The quantitative analysis of the size distribution for the ZnO NPs was achieved by plotting the histogram in **Figure 3C** and **4C**. The size distribution of UZ and DZ (1.0 mol% Ag) NPs is given by mean standard deviation (SD), which can be produced from fitting the histogram using the normal function [solid brown line in **Figures 3C** and **4C**]. The estimated values of D of the samples UZ and DZ (1.0 mol% Ag) NPs are 22 and 24 nm, respectively (**Table 1**). It is evident that the estimated D from HR-TEM images is in good agreement with the D estimated from the XRD patterns. The lattice fringe (**Figures 3D** and **4D**) gives interlayer spacing of 0.22 and 0.24 nm, which corresponds to the d-spacing of (101) plane ( $d_{101} = 0.203$  and 0.247 nm from XRD calculation for UZ and DZ (1.0 mol% Ag) NPs, respectively. Some small black dots are shown in **Figure 4A**, which can be indicated to the Ag NPs. The size distribution of Ag NPs was obtained from fitting the histogram using the normal function [solid red line in **Figure 5**]. The estimated value of Ag NPs size is 3.55 nm (quantum dots). The size and the agglomeration of Ag NPs can produce shift in the Fermi level, and therefore, the recombination of the accumulated electrons with the oxidized redox electrolyte and/or dye species will change [13]. LSPR is barely dependent on the NPL; near-field plasmonic enhancement increases significantly with decreasing particle size [13]. Metal plasmon must be 16 nm in size to escape recombination and produce enhanced photovoltaic parameters [15]. Another



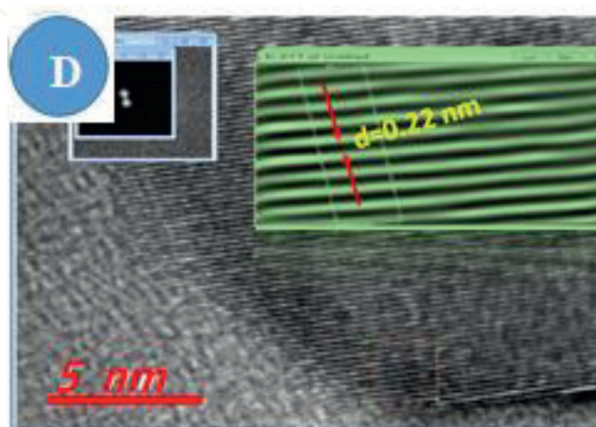
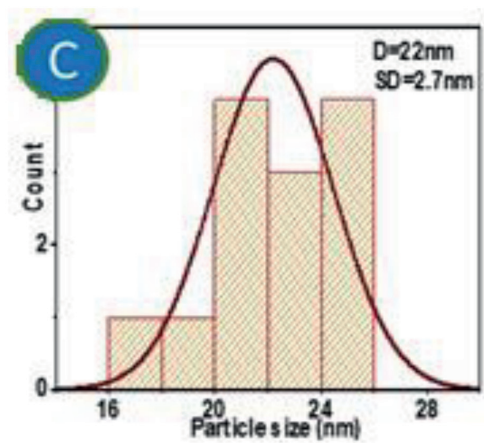
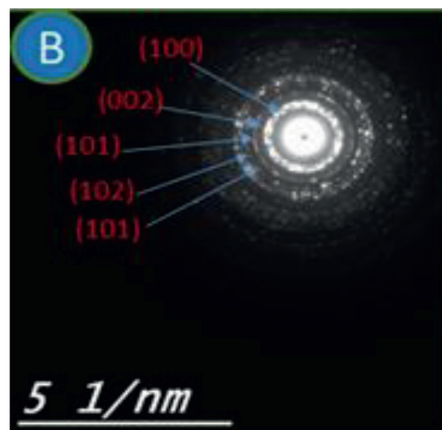
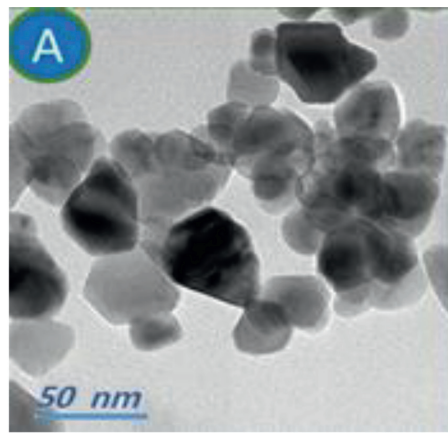


**Figure 3.** HR-TEM micrograph of sample UZ NPs (A) micrograph image, (B) diffraction patterns, (C) histograms, and (D) selected electron diffraction area.

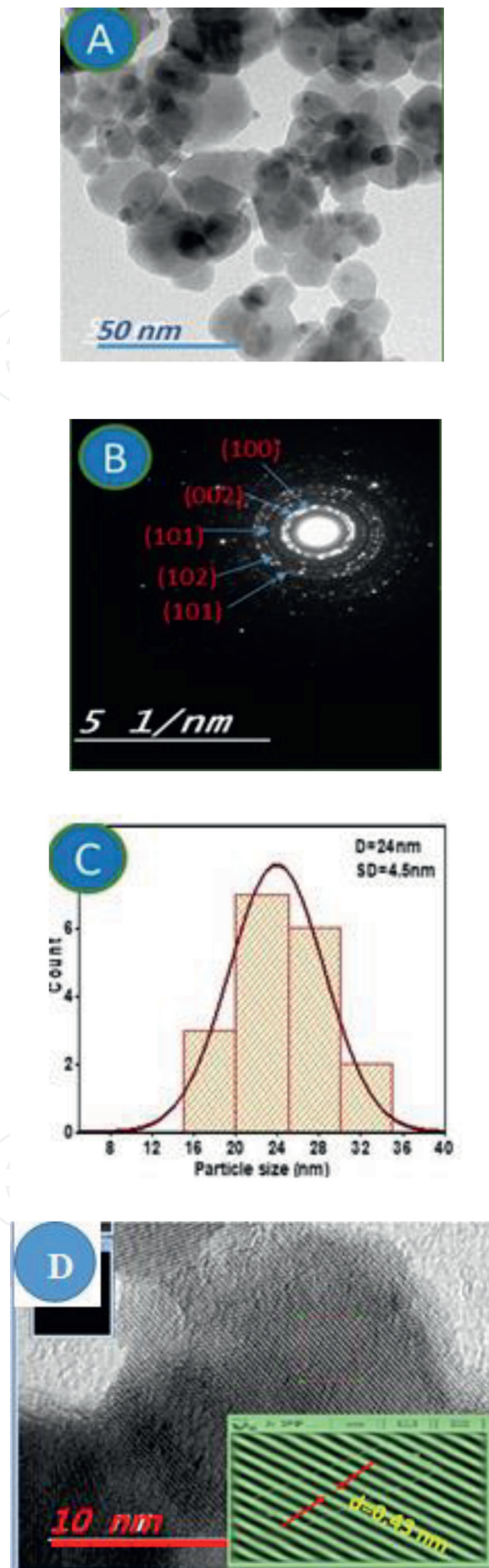


**Figure 4.** HR-TEM micrograph of sample DZ (1.0 Mol% Ag) NP (A) micrograph image, (B) diffraction patterns, (C) histograms, and (D) selected electron diffraction area.

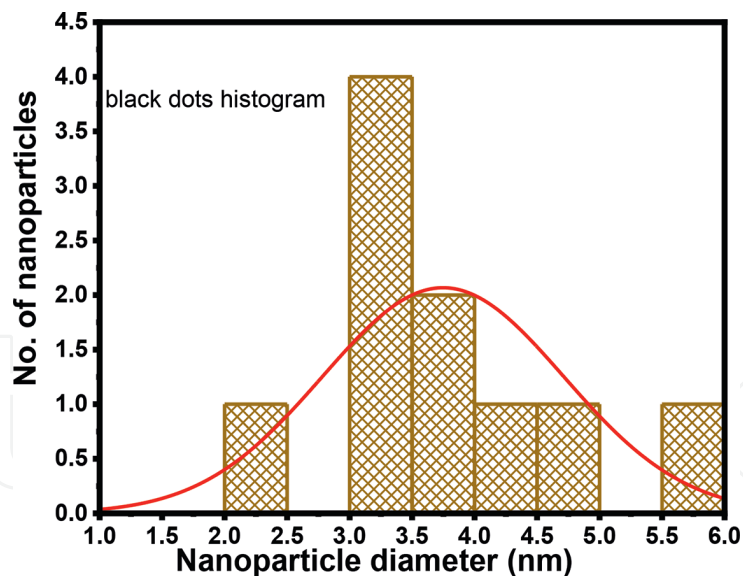


**Figure 5.**  
Histogram of black dot sample DZ (1.0 Mol% Ag) NPs.

study has shown that smaller plasmonic Ag NPs, with an average diameter less than 25 nm in the intrinsic size regime, would exhibit an increased plasmon bandwidth [11]. Conversely, as the Ag NPs size became larger (32 nm), Ag NPs easily aggregated and formed islands. This could not preferentially attach to specific sites on the MO surface, resulting in the decrease of catalytic activity, thereby reducing the reaction rate between MO/dye [15]. In addition, as the thickness of the film is around 32 nm, the mixed films might result in blockage of sunlight which would prevent the incident light from reaching the MO NPs effectively, resulting in the decrease in the photocurrent density.

### 3.3 Optical absorbance and bandgap

**Figure 6** displays typical optical absorption spectra for the as-synthesized samples UZ and DZ NPs. It is clear that the samples have a very high absorbance in the UV region. They decrease exponentially with increasing of the wavelength in the visible region. An enhance photon absorption can be noted in the visible region in

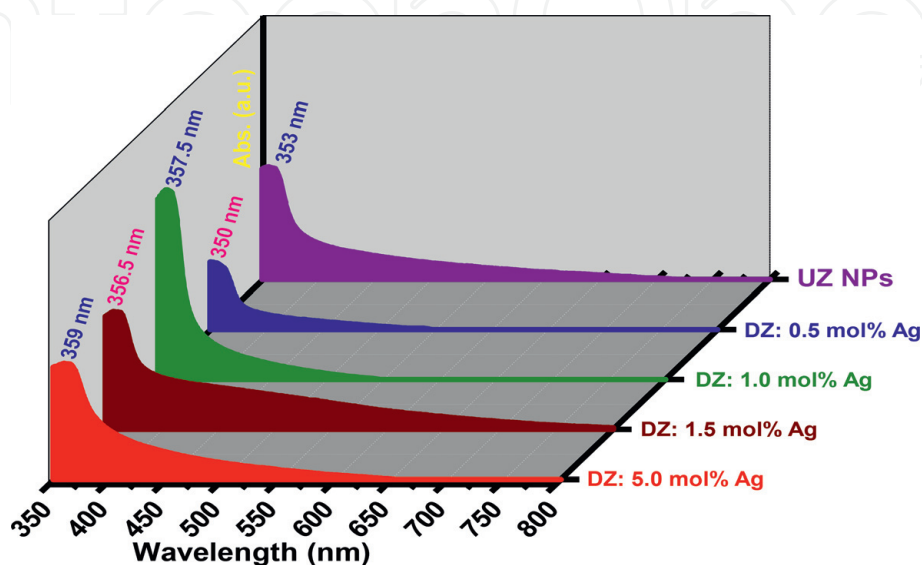


**Figure 6.**  
UV-Vis spectra of UZ and DZ NPs.

the presence of Ag NPs. Furthermore, the highest absorption band can be observed over the range of 350–359 nm, which is ascribed to the band-to-band transition of the ZnO NPs [24]. This exciton absorption peak is being less than of the bulk ZnO (388 nm) which indicates the monodispersing of ZnO NPs as suggested by Brintha et al. [25]. The edge of allowed direct optical bandgap energy ( $E_g$ ) of UZ and DZ NPs was determined using the Tauc Davis and Mott Equation [26]:

$$(h\nu)^2 = S(h\nu - E_g) \quad (3)$$

where  $S$  is constant,  $\alpha$  is the absorption coefficient of the material, and  $h\nu$  (eV) =  $1239.7/\lambda$  (nm) is the photon energy.  $E_g$  was estimated by plotting  $(\alpha h\nu)^2$  versus  $h\nu$  as shown in **Figure 7**.  $E_g$  of UZ and DZ NPs were estimated by extrapolating the linear region to the abscissa, i.e.,  $(\alpha h\nu)^2 = 0$ , yielding  $E_g = 3.21$  to  $3.31$  eV. The estimated energy bandgaps agreed well with the obtained results in Türkylmaz et al. [27]. It can be seen that the addition of Ag NPs decreased the  $E_g$  of ZnO (the inset of **Figure 7**). This implies that the presence of Ag NPs has downshifted the Fermi level of ZnO toward the valence band [1]. As a result, the driving force for electron injection from dye-excited state to ZnO conduction band is increased [1].

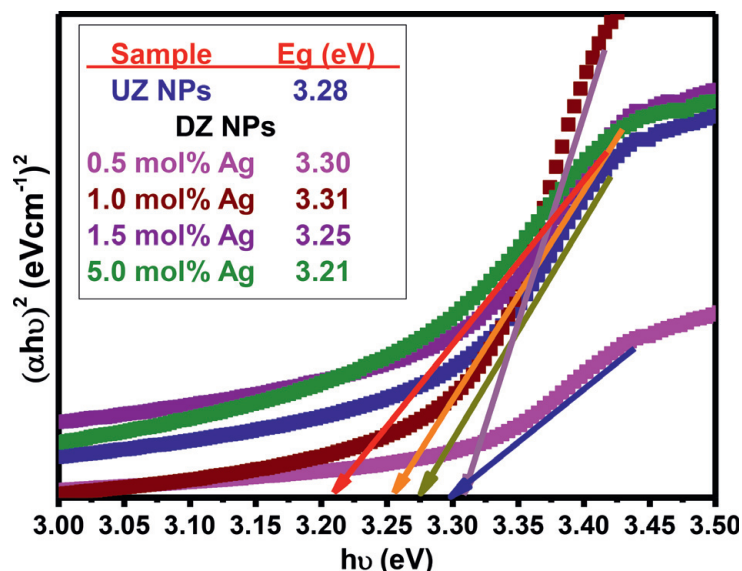


**Figure 7.**  $(\alpha h\nu)^2$  versus photon energy ( $h\nu$ ), the inset is the estimated values of  $E_g$ .

### 3.4 Photoluminescence study

It is well-known that the PL technique is one of the best optical methods for probing electron transitions between high- and low-energy levels as well as for finding electron densities of states [28]. On one hand, it can harness in the material science to identify defects and traps in materials, as well as to estimate the bandgaps of materials. Typically, the PL emission (PLE) spectrum of ZnO NPs exhibits a linear emission in the near ultraviolet (NUV) range (originating from exciton mechanism) and in the visible region (nonradioactive recombination) that is frequently originated from several, intrinsic, and extrinsic defects of ZnO NPs [29]. Different defects or interior energy traps (IETs) can be found within the bandgap of the ZnO NPs, such as vacancies, impurities, imperfections, interstitials, Zn residues, and antisites, mainly from various oxygen vacancies [30, 31]. It is worthy to mention that these IETs play a crucial role in various applications such as the performance of the DSSCs. Therefore, it is hard to recognize the IETs that may be produced, simultaneously, during the synthesization method [29]. **Figure 8**



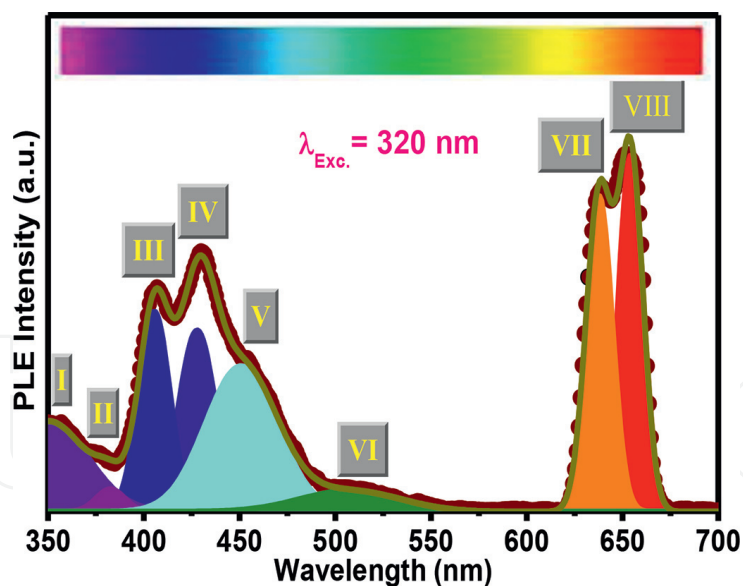


**Figure 8.**  
PLE spectrum and deconvoluted peaks of UZ NPs was excited at 320 nm.

demonstrates the room temperature PLE spectrum of the as-synthesized UZ, which was registered at excitation wavelength of 320 nm at room temperature. The deconvolution of the PLE spectrum recognizes eight peaks (I to VII) as shown in **Figure 8**. The main features of the PLE spectrum of UZ NPs can be resolved into two divisions: NUV and visible. For the PLE spectrum (peak I) of NUV region or the near band edge (NBE) transition, it is designated to the radiative recombination of free excitons through an exciton-exciton collision process [32]. The intensity of such NBE excitonic emission depends on the size of the exciton binding energy of ZnO [33]. Different kinds of IETs are supposed to elucidate the observed transition in the visible range. The transition at peak II is allocated to the movement of the excited electrons from the donor (bottom) of conduction band to the acceptor energy level of Zn vacancy (VZn), which concludes that the ZnO NPs are n-type semiconductors [34], whereas peak III is produced by the transition of electrons from conduction band edge to the IETs complex (VZnO) [28], while peak IV is created by the transition of electrons from interstitial of (Zni) to the IETs complex (VZnO). However, the peak V is originated from transition of electrons from conduction band edge to the IETs complex OZn. The transition at peak VI is ascribed to deep IETs (a shallow surface defect level) of electrons from conduction band edge to the IETs complex vacancies of oxygen (VO). Ultimately, peak VII is attributed to the transition of electrons from interstitial of (Zni) to the IET complex (VO). The center, width, and area of the fitted peaks for the PLE spectrum and the corresponding energy for each peak are tabulated in **Table 2**. As shown in this table, the emission of the visible region is overshadowing NBE transition. The percentage areas of the NBE and the IETs transitions are an indicator of the quality of ZnO (i.e., the ratio of the defects in the ZnO). This is very imperative to facilitate the usage of the ZnO such as DSSCs; a high ratio of defects (IETs transition) is required. This indicates that the defects in ZnO NPs are large, which is deduced from the XRD analysis. Generally, FWHM of intrinsic emission in PL spectrum is related to the crystal quality. A small FWHM indicates that the crystal is of high quality, and its large value suggests that the crystal is imperfect, showing it may have point defects. Meanwhile, at FWHM, the values for both samples are nearly close to each other [35]. The schematic energy band diagram of the PLE spectrum constructed from the data is illustrated in **Figure 9**. The comparative room temperature PLE spectra (excitation at 320 nm) of DZ:1.0 mol% Ag NPs are shown in **Figure 10**. PLE spectrum of DZ:1.0 mol% Ag NPs is used to verify the quality crystal and possible

| Peak # | Center (nm) | Energy (eV)<br>=1239.7/Center | Width (nm) | Height (a.u.) | Area      | Normalized area% |
|--------|-------------|-------------------------------|------------|---------------|-----------|------------------|
| I      | 350.223     | 3.540                         | 40.938     | 45.426        | 9395.400  | 14.194           |
| II     | 382.585     | 3.240                         | 14.725     | 183.117       | 838.326   | 01.267           |
| III    | 405.491     | 3.057                         | 6.116      | 403.887       | 8157.638  | 12.324           |
| IV     | 427.827     | 2.898                         | 18.833     | 365.869       | 8635.687  | 13.046           |
| V      | 450.922     | 2.749                         | 37.306     | 293.802       | 13736.875 | 20.753           |
| VI     | 508.012     | 2.044                         | 52.285     | 42.542        | 2787.723  | 04.212           |
| VII    | 637.758     | 1.944                         | 13.689     | 637.142       | 10931.550 | 16.515           |
| VIII   | 654.309     | 1.895                         | 13.001     | 718.651       | 11709.966 | 17.691           |

**Table 2.**  
 Center, energy, width, height, and area of the measured PLE spectrum of UZ NPs.

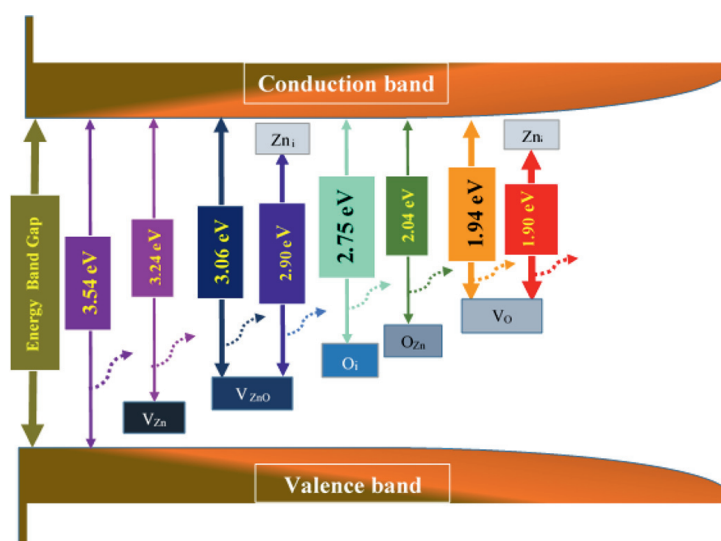


**Figure 9.**  
 Schematic energy band diagram from PLES spectra.

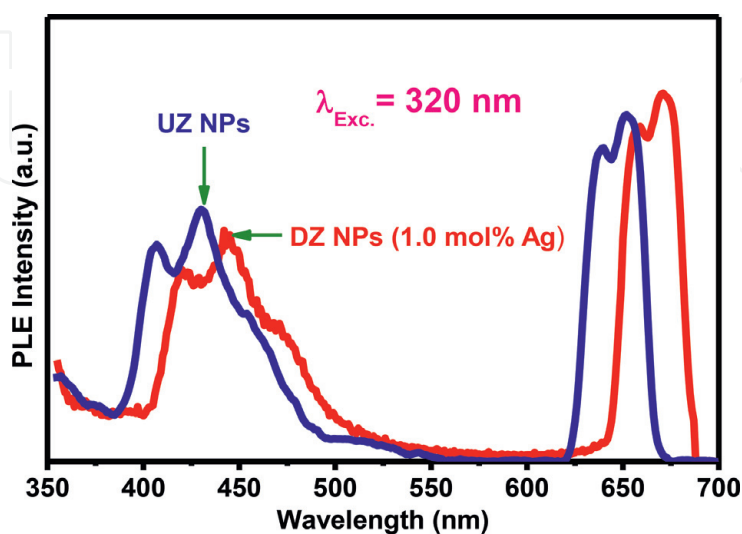


**Figure 10.**  
 PLE spectrum for UZ and DZ:1.0 Mol% Ag NPs was excited at 320 nm.

effects of DZ:1.0 mol% Ag NPs [36]. It is worthy to mention that the intensity and the position of the PLE spectrum DZ:1.0 mol% Ag NPs are dependent on different factors such as the concentration of the noble metal dopants, temperature,

compressive strain, tensile strain, and shape of the particle. It is reported that the decrease in UV intensity was due to the interactions between the excited ZnO NPs and Ag NPs in the grain boundaries, which created a large amount of defects, as confirmed [37]. These kinds of interactions via the Schottky contact, metal–semiconductor diode effect decrease the recombination of electrons and holes generated from UV light irradiation and improved the photocatalytic activities [37]. It could be seen from the PLE spectra that the UV emission in DZ:1.0 mol% Ag NPs decreases which indicates the decrease in electron–hole recombination. This decrease in emission intensity is in accordance with the Stern-Volmer quenching, and similar results were previously reported [35]. The intensity of visible emission initially decreases for 0.5% nominal silver doping and then increases for higher Ag concentrations. Such anomalous intensity variation in Ag-doped ZnO NPs can be understood considering the Ag incorporation process in the NPs. The Ag<sup>+</sup> ions can be incorporated into the ZnO NPs in two different ways: substituting Zn<sup>2+</sup> ions creating doubly ionized oxygen vacancies VO<sup>••</sup> or incorporating as interstitials (Ag<sub>i</sub>) [36]. In addition, PL intensity decreases with increasing amount of Ag doping, indicating that the core of Ag NPs captures the excited electrons before they recombine, causing the so-called electron-sink effect. This causes the accumulation of electrons on the Ag NPs, which improves electron life time and can thus reduce charge recombination, ultimately, improving electron transport [6]. While for low doping concentrations, e.g., 0.5%, most of the incorporated Ag<sup>+</sup> ions might occupy ZnO lattice through Zn<sup>2+</sup> ion substitution; for higher concentrations, the excess amount of Ag<sup>+</sup> ions is incorporated into the NPs interstitially, creating larger amount of lattice defects [36]. By increasing Ag concentration, the intensity of defect decreased. The reduction of defects with Ag doping represented a decline in the defects and improved crystallization [37], which agreed well with XRD results. Compared to the PLE spectra of UZ NPs and DZ:1.0 mol% Ag NPs, it reveals a red-shift (longer wavelength) which is consistent with previous observations [38, 39]. This shift was due to the variation of the energy bandgap of UZ NPs [40], which agree with the UV–Vis results. The dopant Ag has a great effect on the separation and recombination process of photo-induced charge carriers of ZnO, which can further effect on PL performance [41]. It indicates that the PLE mechanism of Ag-doped/ZnO is very complex, and further research is needed.

### 3.5 Photovoltaic performance

The radiant light can be enhanced after being effectively coupled with plasmon absorption due to the increase of the optical density around Ag NPs. According to that, there were more photons, which were usually absorbed by the dye molecules placed in the vicinity of Ag NPs, resulting in the improvement of the device performance [23]. The system so constructed therefore provides a more efficient charge-transfer process with enhanced light absorption, thus leading to a better overall performance of Ag NPs photoanode [11]. The performance of the UZ and DZ NPs photoanodes that were sensitized by EY dye was scanned from 0 to 0.6 V. The characteristic photocurrent density-voltage (J-V) curves of different fabricated DSSCs devices are plotted in **Figure 11**. The calculated values of the photovoltaic performance parameters (efficiency ( $\eta$ ), fill factor (FF), maximum power (P<sub>m</sub>), maximum voltage (V<sub>m</sub>), maximum current density (J<sub>m</sub>), open-circuit voltage (V<sub>OC</sub>), and short circuit photocurrent density (J<sub>SC</sub>)) for all fabricated DSSC devices are plotted in **Figure 12**. The cell with the doped photoanode DZ:1.0 mol% Ag exhibited the highest  $\eta$  and best performance, which has the following performance parameters: V<sub>oc</sub> = 0.46 V, J<sub>sc</sub> = 7.81 mA.cm<sup>-2</sup>, P<sub>m</sub> = 1.91, FF = 51%, and  $\eta$  = 1.91% (**Figure 12**). Through small additions of metal nanostructures (<2 wt %), the active

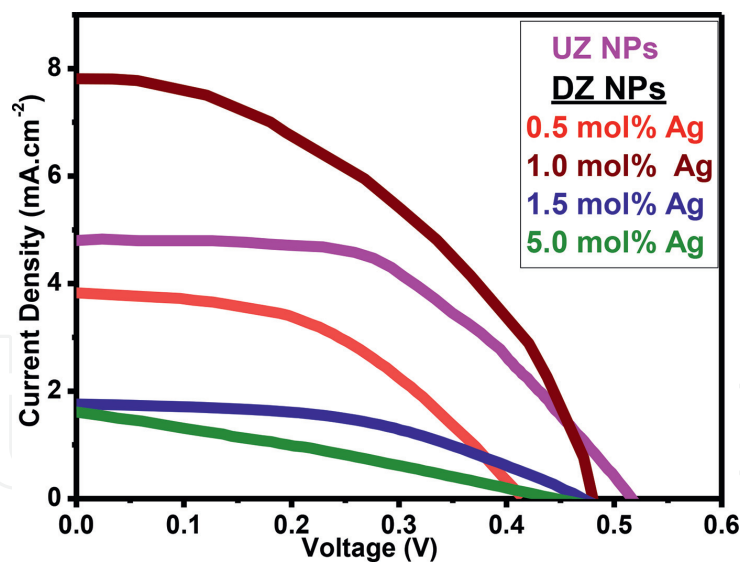


**Figure 11.**  
*J-V behavior for DSSCs based on UZ and DZ NPs photoanode sensitized with EY.*

material required to achieve high efficiency solar conversion can be drastically reduced [5]. However, when the concentration was increased further, the photocurrent decreased, presumably because the Ag NPs act as recombination sites of excited electrons [14]. Consequently, to maximize the plasmonic effect in DSSCs, the optimal concentration of the plasmonic structure was decided to be 0.5 wt% [14]. Previously, it is reported that plasmon-enhanced dye excitation by an electromagnetic field decreased as the distance between dye molecules and plasmonic nanoparticles increased [14]. The enhanced  $J_{sc}$  is related to the light-harvesting capability of dye molecules by plasmon-enhanced excitation [14]. Decrease in  $J_{sc}$  and photon-to-current efficiency beyond 1.0 mol% Ag NPs can also result in a loss of absorbing dye volume due to the large volume of Ag NPs.

In addition, aggregation of Ag NPs may also occur resulting in electron trapping [1]. This process would diminish the electron density, thus decreasing  $J_{sc}$  [1]. This is probably due to plasmonic-induced photocurrents, in that the hot electrons driven from the plasmon-induced charge separation of Ag NPs can be injected into the conduction band of ZnO, resulting in plasmon-assisted photocurrent generation [14]. The improved  $J_{sc}$  is resulted from higher plasmon resonance effect caused by coverage of Ag NPs on the ZnO NPs, which increases the number of photoelectrons generated and improves the effective separation of electron-hole pairs. Therefore, the loaded Ag nanoparticles can improve  $J_{sc}$  rather than the  $V_{oc}$  in these DSSCs. Interestingly, the efficiency of DSSC based on Ag-modified ZnO NPs array decreases again. Such agglomeration of Ag NPs on ZnO NPs results in less surface area for dye loading as well as ineffective light absorption and charge separation [10]. It can be concluded that the improved  $J_{sc}$  may be attributed to not only the increase in the dye excitation by the effects of NPL associated with near-field enhancement and scattering but also to the generation of additional photocurrent owing to the NPL-induced direct hot-electron transfer from plasmonic structures to MO conduction bands [1]. For the higher concentrations of Ag NPs, it may cluster to form larger Ag NPs groups with lower electron storage capability, reducing  $V_{oc}$  [15]. Consequently, the probability of electrons and holes to recombine may increase, so  $J_{sc}$  and  $V_{oc}$  would decrease. Therefore, some of the Ag NPs in the AgZnO network structure may be corroded by electrolyte and oxidized to Ag + ions [1, 15]. This can also increase the recombination rate that could lead to a reduction in electron density in the conduction band of ZnO [1]. This diminishes the number of charge carriers, thereby acting as recombination centers that could lead to a



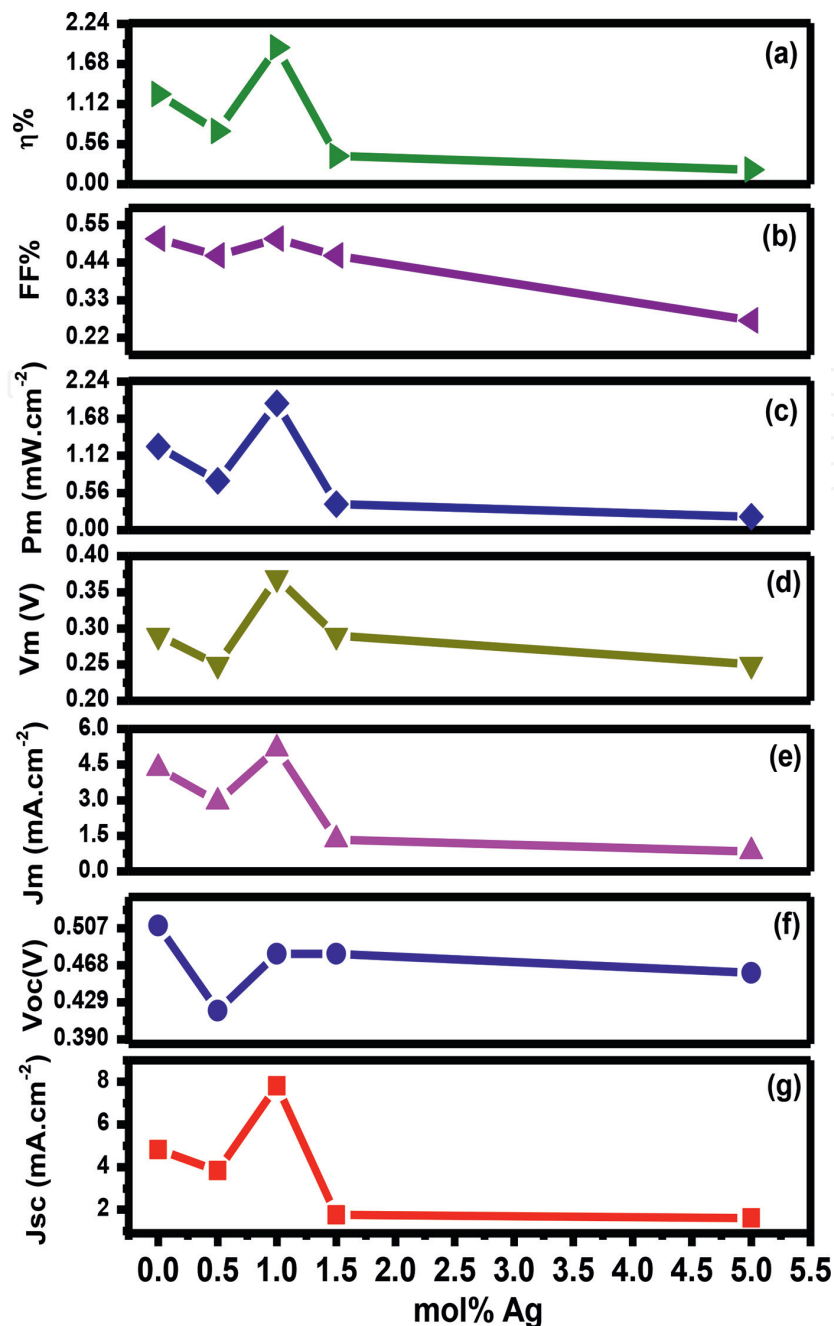


**Figure 12.**

Photovoltaic parameters of UZ and DZ NPs for the DSSCs sensitized with EY dye (a)  $\eta\%$ , (b) FF%, (c)  $P_m$ , (d)  $V_m$ , (e)  $J_m$ , (f)  $V_{oc}$ , and (g)  $J_{sc}$ .

reduction in electron concentration in the conduction band of ZnO, thus resulting in a decrease in  $J_{sc}$  and  $V_{oc}$  [1, 15]. There are contradictory reports on the increase or decrease in the  $V_{oc}$  value induced by the presence of metal NPs in the photoanode [14]. Furthermore, in the case of a further decrease in  $V_{oc}$  as well as FF was observed, it may imply that exposed Ag NPs can act as recombination centers [14].  $V_{oc}$  is typically in proportion to the difference between the quasi-Fermi level and the Nernst potential of the redox couple. Thus, the slight decrease in  $V_{oc}$  can be explained by the downshifted Fermi level due to the incorporation of plasmonic particles [6, 13, 14]. The FF of the fabricated cells changes from 27 to 51% for 5% Ag and 1% Ag, respectively. Generally, the low values of the current density may be attributed to the anchoring group missing in the chemical structure of EY dye. These groups make a strong link between ZnO semiconductor surface and the dye molecule, in order to enhance electron injection from the LUMO energy level of the dye molecule to the conduction band of the semiconductor layer [42]. Nevertheless,

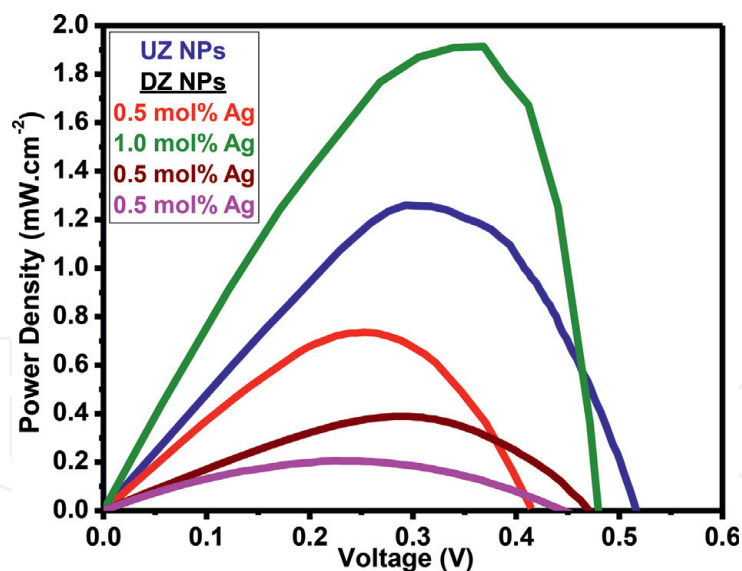


**Figure 13.**  
*Power density for DSSCs based on UZ and DZ NPs photoanode sensitized with EY.*

metallic NPs have been reported to exhibit electron-sink (or photo charging) effect [6]. It was predicted that due to the electron-sink effect of the Ag NPs, a reduction in charge recombination and improved charge transport are evidenced in improving FF value with increasing plasmonic NP doping. Thus, this would account for the slight increase in  $J_{sc}$ . **Figure 13** presents the power density for DSSCs based on UZ and DZ NPs photoanode sensitized with EY.

### 3.6 Transient open-circuit voltage decay measurement

Agreeing to the proposed simple model of the DSSCs by Ref. [43] at short circuit, different charge-transition processes can be found in the DSSCs devices, in which the slower recombination process is preferable. In addition, the charge can present more than one kind of motion status at different voltage-dependent regions. Among them, the exponential increase region relates to internal trapping of the photoanode material, which reveals the apparent electron lifetime or response time ( $\tau_n$ ) or the electron recombination rate ( $k_{rec}$ ) in the photoanode material. The transient open-circuit photovoltage decay (TOCVD) is a suitable method to study  $\tau_n$  and  $k_{rec}$  in DSSC, which can provide some quantitative information on the electron recombination velocity in DSSC [44]. In order to conduct the TOCVD measurement, the DSSCs devices, based on UZ and DZ 1.0 mol% Ag NPs, were illuminated for 2 min to be equilibrium.

Between electron injection and electron recombination at the FTO surface, i.e., a steady-state voltage was obtained and  $V_{oc}$  was recorded after that, the subsequent decay of photovoltage during the light source was turned off. The decay of the photovoltage reflects the decrease of the electron concentration at the FTO surface, which is primarily produced by the charge recombination. In other words, the recombination velocity of photoelectron is proportional to the response of the TOCVD [44]. **Figure 14** depicts TOCVD experiment for the DSSCs devices, which follow a pseudoexponential (semilog) form. Two decayed components are distinguished, fast and slow decays, which may be ascribed to their intrinsic material properties [45]. This, also, may be attributed to the different defects of the ZnO NPs that were proved in the PL results earlier. A double exponential function was used as a powerful fitting function for the TOCVD data as depicted in Eq. (4) to extract the decay parameters [24]:

$$V_{OC} = V_0 + V_1 e^{-\frac{(t-t_0)}{\tau_1}} + V_2 e^{-\frac{(t-t_0)}{\tau_2}} \quad (4)$$

where  $V_0$  is the offset of the  $V_{OC}$ . The amplitudes of VOC for fast and slow decay are  $V_1$  and  $V_2$ , respectively; it is the decay time and is the center of the fitting curve. The decay time constant (lifetime) for fast curve and slow curve is  $\tau_1$  and  $\tau_2$ , respectively. For the right-hand side of Eq. (4), it describes the fast and slow decays, respectively, the second term for the fast decay and the third term for the slow decay [24]. All extracted decay parameters of the TOCPV are listed in **Table 3**. As it was reported in Ref. [24], the  $k_{rec}$  is determined by

$$k_{rec} = \left[ \frac{V_1}{\tau_1} e^{-\frac{(t-t_0)}{\tau_1}} + \frac{V_2}{\tau_2} e^{-\frac{(t-t_0)}{\tau_2}} \right] (V_T)^{-1} \quad (5)$$

where the thermal voltage ( $V_T = K_B T/q$ ), with  $K_B$ , is Boltzmann constant,  $T$  is the absolute temperature, and  $q$  is the elementary charge, using the following Equation [36]

$$\tau_n = -V_T \left( \frac{dV_{os}}{dt} \right)^{-1} \quad (6)$$

Meanwhile, the recombination rate of the device based on DZ:1.0 mol% Ag NPs photoanode is slower than that of UZ NPs photoanode. The results revealed that the  $\tau_n$  in the UZ NPs photoanode-based DSSC was longer than that in the DZ:1.0 mol% Ag NPs photoanode-based DSSCs, demonstrating that the latter possessed a higher

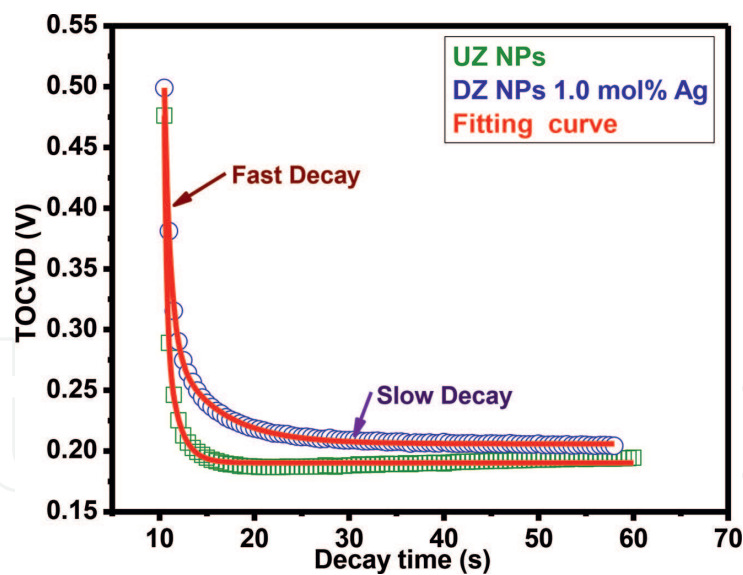


**Figure 14.** TOCPVD of the DSSCs cells is the sensitized EY based on UZ and DZ 1.0 Mol% Ag NPs, and the red line is the double exponential decay fitted curve.

| Decay parameters | $V_0$ (V) | $t_0$ (s) | Fast decay |              | Slow decay |              | $\tau_n$ (s) | $k_{rec}$ (s) <sup>-1</sup> | $R^2$ |
|------------------|-----------|-----------|------------|--------------|------------|--------------|--------------|-----------------------------|-------|
|                  |           |           | $V_1$ (V)  | $\tau_1$ (s) | $V_2$ (V)  | $\tau_2$ (s) |              |                             |       |
| UZ               | 0.190     | 10.471    | 0.194      | 0.244        | 0.115      | 1.294        | 1.538        | 0.650                       | 0.993 |
| 1.0 mol% Ag      | 0.206     | 10.448    | 0.227      | 0.651        | 0.085      | 5.096        | 5.747        | 0.174                       | 0.991 |

**Table 3.**  
The parameters of the TOCPVD.

surface trap density [45] that might result from the larger surface area. The higher recombination rate and shorter electron lifetime within ZnO NPs photoanode were the reason why the FF of the corresponding DSSCs decreased.

### 3.7 Dye absorption spectrum

A major problem, however, is the attachment of less dye, reducing the J. One approach to solve this problem is based on a plasmonic structure, such as silver (Ag NPs), gold (Au NPs), or gold nanorods [10]. **Figure 15** displays the UV–Vis absorption spectra of one derivative of EY dye, which was dissolved in absolute ethanol. It is clear that the maximum absorption peak of EY is positioned at 526 nm; also, other small peak is located at 309 nm. EY exhibits a powerful absorption peak in the visible region, and its spectrum covers broader window than the others. The intensity of the observed absorption peaks in testing rang represents a part of energy losses in the transition in the UV region. In the DSSC application, it is much of interests to concentrate in the visible solar spectrum. In addition to that, the molar extinction coefficient of EY equals  $112,000 \text{ (cmM)}^{-1}$ , corresponding to  $\pi \rightarrow \pi^*$  transitions of conjugated molecules [46, 47]. To investigate the effect on the light absorption enhancement of dye molecules of the DSSCs photoanode, the optical absorbance was measured of dye-sensitized plasmonic NP composite-embedded photoanode and compared them to that of the reference UZ photoanode. The results are shown in **Figure 16**. The relatively broad and strong enhancement is observed in the range of 250–550 nm with a maximum enhancement around 307 nm, which coincides with the absorption band position of decorated Ag NPs. These features suggest that dye molecules in the vicinity of Ag NPs can absorb more photons, presumably due to the intensified near-field effect of the surface plasmon and spectral overlap between the dye and plasmon, which may eventually lead to an increase in the number of charge carriers and Jsc values [14]. The plasmonic photoanode recorded higher absorbance than the pristine photoanode. This is a typical result in many reported works on plasmonic DSSCs [6]. The absorption in the visible region is shifted from 526 to 518.06 nm, as revealed in **Figure 16**. This can be explained by a change in the energy levels of highest occupied molecular orbital (HOMO) and lowest unoccupied molecular orbital (LUMO) of EY compared to those in solution, due to the interaction between EY molecules and the ZnO film

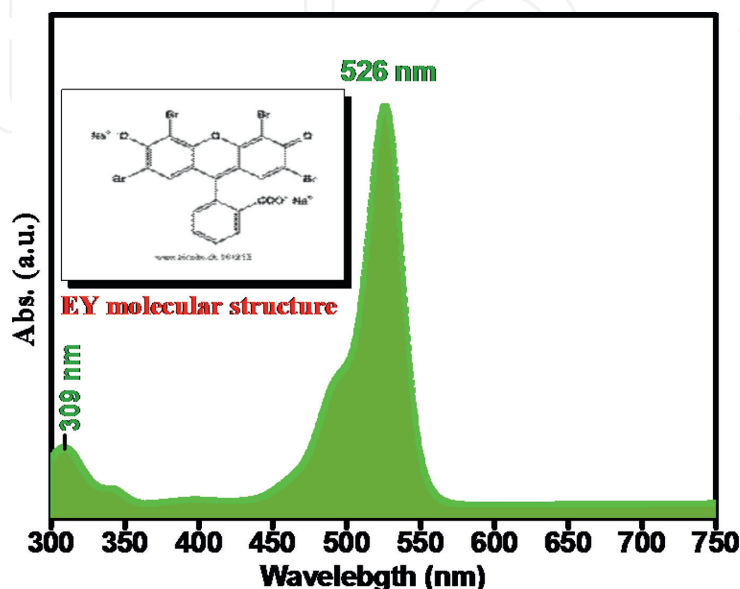


**Figure 15.**  
*UV–Vis absorption spectra of EY dyes dissolved in absolute ethanol.*



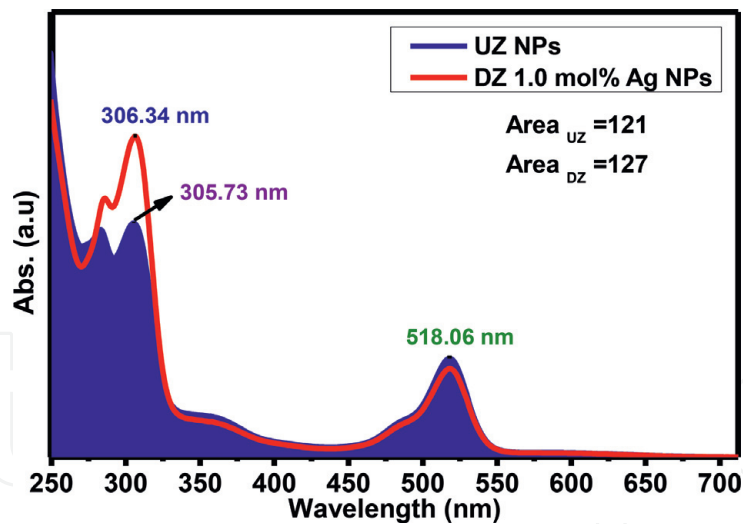


**Figure 16.**  
UV-Vis adsorption spectra of EY dyes absorbed by UZ and DZ 1.0 Mol % Ag NPs.

[48, 49]. These results show a synergistic effect between the dye and plasmonic NPs, on the light absorption enhancement effect [6].

#### 4. Conclusion

Undoped and doped (Ag) ZnO NPs photoanodes were successfully synthesized and mediated by the combustion method. XRD results indicated that a single phase of hexagonal wurtzite structure was formed. The XRD confirmed that no Ag peaks could be observed for 1%. The HR-TEM micrograph showed that semispherical particles (20.45 and 22.30 nm) for ZnO NPs were well crystallized with an intermediate or poor agglomeration. The average ZnO NPs size was confirmed by XRD and HR-TEM inspections. The calculated bandgap of the ZnO NPs was found to be changed with the addition of the Ag<sup>+</sup> ions. The PLE spectrum of the undoped ZnO NPs was examined and decomposed into two divisions: NUV and visible (violet-blue, blue-green, and orange-red). The PLE spectrum changed with the dopant Ag. The DZ:Ag 1.0 mol% dye-sensitized cells presented the best DSSCs performance among others. The results showed an enhancement of efficiency of both the J<sub>sc</sub>, J<sub>m</sub>, V<sub>m</sub>, P<sub>m</sub>, and FF% efficiency and the V<sub>oc</sub> for the (Ag 1.0 mol%) dye-sensitized cells compared to others, which is attributed to the light-harvesting capability of dye molecules by plasmon-enhanced excitation. In addition, the recombination rate of the device based on DZ:1.0 mol% Ag NPs photoanode was slower than that of UZ NP photoanode. The lower recombination rate and shorter electron lifetime within the ZnO NP photoanode were the reason why the FF of the corresponding DSSCs increased.

#### Acknowledgements

The authors would like to thank the Palestinian German Joint Research Project PALGER2015-34-012 and the PHC Al Maqdisi grant No. 37038WF for their partially financial support of this research. The authors would, also, like to thank Mr. Ahmad Ashour for his technical assistant.

#### Conflict of interest

Authors confirm that there are no conflicts of interest.

# IntechOpen

## Author details

Samy K.K. Shaat<sup>1\*</sup>, Hussam Musleh<sup>2</sup>, Jihad Asad<sup>2</sup>, Nabil Shurrab<sup>3</sup>, Ahmed Issa<sup>4</sup>, Amal AlKahlout<sup>2</sup> and Naji Al Dahoudi<sup>2</sup>

1 Department of Physics, Islamic University of Gaza, Gaza, Palestine

2 Department of Physics, Al Azhar University-Gaza, Gaza, Palestine


3 Department of Chemistry, Al Azhar University-Gaza, Gaza, Palestine

4 Department of Engineering, Al Azhar University-Gaza, Gaza, Palestine

\*Address all correspondence to: [samyshaat@yahoo.com](mailto:samyshaat@yahoo.com)

## IntechOpen

---

© 2019 The Author(s). Licensee IntechOpen. This chapter is distributed under the terms of the Creative Commons Attribution License (<http://creativecommons.org/licenses/by/3.0>), which permits unrestricted use, distribution, and reproduction in any medium, provided the original work is properly cited. 

## References

- [1] Shah S, Noor IM, Pitawala J, Albinson I, Bandara TMWJ, Mellander B-E, et al. Plasmonic effects of quantum size metal nanoparticles on dye-sensitized solar cell. *Optical Materials Express*. 2017;7(6):2069-2083
- [2] Wei Y, Ran L, Hao H, Yujie X. Plasmonic nanostructures in solar energy conversion. *Journal of Materials Chemistry C*. 2017;5:1008
- [3] Nada A. Renewable energy types. *Journal of Clean Energy Technologies*. 2014;2(1):61-64
- [4] Ying-Chih P, Jin Z. Mechanisms behind plasmonic enhancement of photocurrent in metal oxides. *Austin Journal of Nanomedicine & Nanotechnology*. 2014;2(5):1030
- [5] Song DH, Kim HS, Suh JS, Jun BH, Rho WY. Multi-shaped Ag nanoparticles in the plasmonic layer of dye-sensitized solar cells for increased power conversion efficiency. *Nanomaterials*. 2017;7(6):136. DOI: 10.3390/nano7060136
- [6] Pascal N, Go K, Wai T, Hiroyuki M, Atsunori M. Systematic characterization of the effect of Ag@TiO<sub>2</sub> nanoparticles on the performance of plasmonic dye-sensitized solar cells. *Scientific Reports*. 2017;7(1-12):15690. DOI: 10.1038/s41598-017-15541-z.
- [7] Holly Z, William E, Abdelaziz B, Olivia H, Joseph W, Alexander P, et al. Improving light harvesting in dye-sensitized solar cells using hybrid bimetallic nanostructures. *ACS Photonics*. 2016;3(3):385-394. DOI: 10.1021/acsp Photonics.5b00552
- [8] Hua D, Zhaoxin W, Yucui G, Ahmed E, ShuYa N, Jun X, et al. Silver-loaded anatase nanotubes dispersed plasmonic composite photoanode for dye-sensitized solar cells. *Organic Electronics*. 2014;15:2847-2854
- [9] Ahmad M, Pandey A, Rahim N. Towards the plasmonic effect of Zn nanoparticles on TiO<sub>2</sub> monolayer photoanode for dye sensitized solar cell applications. *Materials Letters*. 2017;195:62-65
- [10] Xinning L, Ying W. Plasmon-enhanced performance of dye-sensitized solar cells based on electrodeposited Ag nanoparticles. *Journal of Materials Science and Technology*. 2014;30(1):1-7
- [11] Marwa A, Nafiseh M, Lei Z, Joseph T, Donald M, Saurabh S, et al. Plasmonic gold nanoparticles for ZnO-nanotube photoanodes in dye-sensitized solar cell application. *Nanoscale*. 2016;8:1658
- [12] Vinod K, Swart H, Som S, Vijay K, Yousif A, Anurag P, et al. The role of growth atmosphere on the structural and optical quality of defect free ZnO films for strong ultraviolet emission. *Laser Physics*. 2014;24:105704
- [13] Stafford S, Heeso N, Gary B, Hui C, Charles S. Plasmonic Enhancement Of Dye-sensitized solar cells using core-shell nanostructures. *The Journal of Physical Chemistry C*. 2013;117(2):927-934. DOI: 10.1021/jp311881k
- [14] Yoon J, Yu J, Saji K, Myunghwan B, Zhiqun L, Dong K. Plasmonic dye-sensitized solar cells incorporated with Au-TiO<sub>2</sub> nanostructures with tailored configurations. *Nanoscale*. 2014;6:1823
- [15] Danladi E, Joshua O, Gabriel O, Ezeoke J. Plasmon-enhanced efficiency in dye sensitized solar cells decorated with size-controlled silver nanoparticles based on anthocyanins as light harvesting pigment. *Journal of Photonic*

Materials and Technology. 2016;2(1): 6-13. DOI: 10.11648/j.jmpt.20160201.12

[16] Kumar V, Prakash J, Singh J, Chae K, Swart C, Ntwaeaborwa O, et al. Role of silver doping on the defects related photoluminescence and antibacterial behaviour of zinc oxide nanoparticles. *Colloids and Surfaces B: Biointerfaces*. 2017;1(159):191-199. DOI: 10.1016/j.colsurfb.2017.07.071.

[17] Rad M, Kompany A, Zak A, Abrishami E. The effect of silver concentration and calcination temperature on structural and optical properties of ZnO:Ag nanoparticle. *Modern Physics Letters B*. 2015;29(1): 1450254. DOI: 10.1142/S0217984914502546

[18] Vinod K, Swart H, Ntwaeaborwa O, Kroon R, Terblans J, Shaat SKK, et al. Origin of the red emission in zinc oxide nanophosphors. *Materials Letters*. 2013; 101:57-60

[19] Talaat JKS, Hammad M, Roger H. The influence of annealing temperature on the structure, morphologies and optical properties of ZnO nanoparticles. *Superlattices and Microstructures*. 2010; 47:335-340

[20] Zhou X, Xie Y, Mi H, Ma J, Yang J, Cheng J. Comparative study of two methods for the synthesis of CuBi<sub>2</sub>O<sub>4</sub> particles and their application in ZnO-based dye-sensitized solar cells. *Journal of Materials Science: Materials in Electronics*. 2017;28:13437-13444

[21] Zayed H, Musleh H, Shaat SKK, Shurrab N, Asaad J, AlDahoudi N. Synthesis of zinc oxide nanoparticles at different aging time for low cost dye sensitized solar cells. *Journal of Scientific Research in Science*. 2018;34: 275-286

[22] Salem J, Hammad T, Kuhn S, Draaz M, Hejazy N, Hempelmann R.

Structural and optical properties of Co-doped ZnS nanoparticles synthesized by a capping agent. *Journal of Materials Science: Materials in Electronics*. 2014; 25:2177-2182

[23] Van-Duong D, Ho-Suk C. Highly-efficient plasmon-enhanced dye-sensitized solar cells created by means of dry plasma reduction. *Nanomaterials*. 2016;6(4):70. DOI: 10.3390/nano6040070

[24] Shaat SKK, Zayed H, Musleh H, Shurrab N, Issa A, Asad J, et al. Inexpensive organic dyes-sensitized zinc oxide nanoparticles photoanode for solar cells devices. *Journal of Photonics for Energy*. 2017;7:025504-025504

[25] Brintha S, Ajitha M. Synthesis and characterization of ZnO nanoparticles via aqueous solution, sol-gel and hydrothermal methods. *IOSR Journal of Applied Chemistry*. 2015;8(11):66-72

[26] Shaat SKK, Swart H, Ntwaeaborwa O. Investigation of luminescent properties of Ca<sub>0.3</sub>Sr<sub>0.7</sub>Al<sub>2</sub>O<sub>4</sub>:Tb<sup>3+</sup>,Eu<sup>3+</sup> excited using different excitation sources. *Journal of Electron Spectroscopy and Related Phenomena*. 2014;197:72-79

[27] Türkyılmaz ŞŞ, Güy N, Özacar M. Photocatalytic efficiencies of Ni, Mn, Fe and Ag doped ZnO nanostructures synthesized by hydrothermal method: The synergistic/antagonistic effect between ZnO and metals. *Journal of Photochemistry and Photobiology A: Chemistry*. 2017;341:39-50

[28] Jin-Han L, Ranjit P, Rupesh D, Zhe-An L, Yi-Ping W, Ching-Hwa H, et al. Photoluminescence mechanisms of metallic Zn nanospheres, semiconducting ZnO nanoballoons, and metal-semiconductor Zn/ZnO nanospheres. *Scientific Reports*. 2014; 4(6967):1-8



- [29] Manoranjan G, Raychaudhuri A. Shape transition in ZnO nanostructures and its effect on blue-green photoluminescence. *Nanotechnology*. 2008;**19**(44):445704
- [30] Nanda S, Asit P, Tapendu M, Monica K. Processing temperature dependent morphological and optical properties of ZnO nanorods. *Materials Science in Semiconductor Processing*. 2014;**20**:55-60
- [31] Karkeng L, Muhammad H, Roslinda S, Al-Hardan NH, Ishak M, Weesiong C. Temperature-driven structural and morphological evolution of zinc oxide nano-coalesced microstructures and its defect-related photoluminescence properties. *Materials*. 2016;**9**(4):300-315
- [32] Irimpan L, Nampoori VPN, Radhakrishnan P. Size dependent fluorescence spectroscopy of nanocolloids of ZnO. *Journal of Applied Physics*. 2007;**102**:063524
- [33] Chang K, Pyung M, Sungyeon K, Jae M, Hyeon J, Jungsik B, et al. Effect of carrier concentration on optical bandgap shift in ZnO:Ga thin films. *Thin Solid Films*. 2010;**518**(22):6304-6307
- [34] Aneesh PM, Vanaja KA, Jayaraj MK. Synthesis of ZnO nanoparticles by hydrothermal method. *Proceedings of SPIE*. 2007;**6639**:66390J
- [35] Shah AH, Manikandan E, Ahmed M, Ganesan V. Enhanced bioactivity of Ag/ZnO Nanorods-a comparative antibacterial study. *Journal of Nanomedicine & Nanotechnology*. 2013;**4**:3
- [36] Zeferino R, Flores M, Pal U. Photoluminescence and Raman scattering in Ag-doped ZnO nanoparticles. *Journal of Applied Physics*. 2011;**109**:014308. DOI: 10.1063/1.3530631
- [37] Hosseini SM, Sarsari I, Kameli P, Salamati H. Effect of Ag doping on structural, optical, and photocatalytic properties of ZnO nanoparticles. *Cond-mat.mtrl-sci*. 2015:1-13. rXiv: 1508.00382v1. DOI: 10.1016/j.jallcom.2015.03.136
- [38] Kuznetsov AS, Lu Y-G, Turner S, Shestakov V, Tikhomirov VK, Kirilenko D, et al. Preparation, structural and optical characterization of nanocrystalline ZnO doped with luminescent Ag-nanoclusters. *Optical Materials Express*. 2012;**2**(6):723
- [39] Oleg L, Vasilii C, Vasile P, Mahdi ABRC, Lee C, Ion T, et al. Silver-doped zinc oxide single nanowire multifunctional nanosensor with a significant enhancement in response. *Sensors and Actuators B*. 2016;**223**:893-903
- [40] Gem T, Rhituraj S. A review on the optical properties of ZnO nanostructures for optoelectronic device application. *International Journal of Management, Technology and Engineering*. 2546;**8**(XI):2018
- [41] Nguyen N, Tran T, Nguyen T, Doan T. Preparation and characterization of silver doped ZnO nanostructures. *Open Journal of Synthesis Theory and Applications*. 2012;**1**:18-22
- [42] Calogero G, Bartolotta A, Marco G, Carlo A, Bonaccorso F. Vegetable-based dye-sensitized solar cells. *Chemical Society Reviews*. 2015;**44**:3244-3294
- [43] Zhang Z. École polytechnique fédérale de lausanne [PhD thesis]. Switzerland; 2008
- [44] Fabregat-Santiago F, García-Cañadas J, Palomares E, Clifford JN, Haque SA, Durrant JR, et al. The origin of slow electron recombination processes in dye-sensitized solar cells with a

lumina barrier coatings. *Journal of Applied Physics*. 2004;**96**:6903-6907

[45] Chengkun X, Paul S, Liangliang C, Jiamin W, Di G. Ordered TiO<sub>2</sub> nanotube arrays on transparent conductive oxide for dye-sensitized solar cells. *Chemistry of Materials*. 2010;**22**(1):143-148. DOI: 10.1021/cm9027513.

[46] Musleh H, AlDahoudi N, Zayed H, Shaat SKK, Tamous HM, Shurrab N, et al. Synthesis and characterization of ZnO nanoparticles using hydrothermal and sol-gel techniques for dye-sensitized solar. *Journal of University of Babylon for Engineering Sciences*. 2018; **26**(9):256-267

[47] Shaat SKK, Musleh H, Zayed H, Tamous H, Issa A, Shurrab N, et al. Solution combustion-derived ZnO nanoparticles for photoanode of solar cells. *Materials Science and Engineering B*. 2019;**241**:75-81

[48] Hara K, Horiguchi T, Kinoshita T, Sayama K, Sugihara H, Arakawa H. Highly efficient photon-to-electron conversion with mercurochrome-sensitized nanoporous oxide semiconductor solar cells. *Solar Energy Materials and Solar Cells*. 2000;**64**: 115-134

[49] Rohatgi K, Singhal G. Nature of bonding in dye aggregates. *The Journal of Physical Chemistry*. 1966;**70**: 1695-1701